

Supporting Information-

Identification and Manipulation of Defects in Black Phosphorus

Rishav Harsh,^{†,‡,△} Sourav Mondal,^{¶,§,△} Devina Sharma,^{¶,△} Mehdi Bouatou,[†]
Cyril Chacon,[†] Maxim Ilyn,^{||} Celia Rogero,^{||,⊥} Vincent Repain,[†] Amandine
Bellec,[†] Yann Girard,[†] Sylvie Rousset,[†] Raman Sankar,[#] Woei Wu Pai,[@]
Shobhana Narasimhan,[¶] and Jérôme Lagoute^{*,†}

[†]*Université de Paris, CNRS, Laboratoire Matériaux et Phénomènes Quantiques, 75013,
Paris, France.*

[‡]*Present address: Donostia International Physics Center DIPC, Donostia-San Sebastian,
Basque Country 20018, Spain*

[¶]*Theoretical Sciences Unit and School of Advanced Materials, Jawaharlal Nehru Centre for
Advanced Scientific Research, Jakkur, Bangalore 560064, India*

[§]*Present address: School of Physics, Trinity College Dublin, Dublin-2, Ireland*

^{||}*Centro de Física de Materiales (CFM-MPC) Centro Mixto CSIC-UPV/EHU, E-20018
Donostia-San Sebastian, Spain*

[⊥]*Donostia International Physics Center DIPC, Donostia-San Sebastian, Basque Country
20018, Spain*

[#]*Institute of Physics, Academia Sinica, Taipei 11529, Taiwan, ROC*

[@]*Center for Condensed Matter Sciences, National Taiwan University, Taipei 106 Taiwan,
Republic of China*

[△]*Contributed equally to this work*

E-mail: jerome.lagoute@u-paris.fr

Experimental Methods

Black phosphorus synthesis

Single crystals of BP were synthesized by the reaction of red phosphorus (1 g, 99.99%, powder, Alfa Aesar), tin (0.6 g, 99.999%, granule, Alfa Aesar), gold (0.4 g, 99.999%, granule, Alfa Aesar) and SnI_4 (250 mg, 99.99%, crystalline, Alfa Aesar) in an evacuated silica glass ampoule ($p = 10^{-3}$ mbar, length 400 mm, inner diameter 20 mm and wall thickness 2 mm). The ampoule was placed horizontally in a tube furnace with two zone heating furnaces. The two-step heating synthesis process involved a series of temperature-programmed reactions, constant temperature heating, and slow cooling treatment. In the first-step heating reaction, the reaction starting materials were placed at one side of the silica ampoule and located at the high temperature zone (materials zone) of the furnace. The furnace was heated from room temperature (RT) to 475°C in 12 h, and then kept for 24 h at 475°C. The empty side of the silica ampoule was located at the low temperature zone (growth zone), which was simultaneously heated from RT to 425°C in 12 h. Secondly, the setting temperatures were maintained for 24 h. Subsequently, in the second-step heating reaction, the hot and low temperature zones were further heated to 650°C (materials zone) and 550°C (growth zone) respectively at a slow heating rate of 40°C per hour, and the setting temperatures were maintained for 12 h. After that, the silica glass ampoule was cooled to ambient temperature with a slow cooling rate of 50°C per hour. Finally, we obtained a large size single crystal of BP.

STM Measurements

STM measurements were performed using a low-temperature STM apparatus (Omicron) working at 4.6 K at a pressure lower than 1×10^{-10} mbar. The dI/dV spectra were acquired using a lock-in detector at a frequency of ca. 767 Hz and a modulation amplitude of 35 mV. The measurements were performed with an electrochemically etched tungsten tip. Before

measuring on BP, the tip was calibrated on a Au(111) surface until it showed the Shockley surface state feature in the spectroscopic measurements. All STM topography scans have been taken in the constant current mode unless stated otherwise.

Experimental and calculated STM topography images have been processed in WSxM software¹ without any filtering.

Exfoliation

For the mechanical exfoliation of the sample from a BP crystal, an epoxy (EPOTEK H21D) was used to glue a metallic strip on top of the crystal. After curing the epoxy in ambient conditions, the strip got firmly bonded and the sample was then transferred to an ultra high vacuum chamber. At a pressure lower than 10^{-9} mbar, the strip was knocked off from the sample, thereby peeling off the topmost layers of the bulk crystal, and exposing a fresh surface for tunneling measurements. Cleaved sample was then immediately transferred to the STM chamber (pressure lower than 10^{-10} mbar) for LT measurements without any further annealing.

Computational Methods

Our calculations were performed within the framework of spin polarized density functional theory, using the Quantum ESPRESSO package.^{2,3} The exchange-correlation potential was treated using the Perdew-Burke-Ernzerhof (PBE) form of the generalized gradient approximation (GGA).⁴ We used ultrasoft pseudopotentials to describe the interactions between the ionic cores and valence electrons.⁵ The Kohn-Sham orbitals were expanded in a plane wave basis set, with cutoffs of 35 Ry and 350 Ry for wavefunctions and charge densities, respectively. Long-range dispersion interactions were incorporated using the semi-empirical DFT-D2 technique.⁶

The BP was modeled using a slab model, with three layers stacked along the \mathbf{c} lattice vector, and each layer having dimensions $7\mathbf{a} \times 9\mathbf{b}$. The atoms in the bottom-most phosphorene layer were held fixed, all other atoms were allowed to relax until the forces were less than 10^{-3} Ry/Bohr. Brillouin zone (BZ) sampling was restricted to the zone center for the geometry optimization calculations. To generate the charge density, density of states and STM images, we used a $3 \times 3 \times 1$ \mathbf{k} -mesh to sample the BZ, using the Monkhorst-Pack scheme.⁷ Convergence was aided by using Marzari-Vanderbilt⁸ smearing of width 0.001 Ry. All the constant current STM images were simulated using the Tersoff-Hamann approach,⁹ for the relaxed configuration of the defects.

STM/STS on pristine Black phosphorus

In this work, we study the nature of native defects present in a bulk black phosphorus crystal. The BP surface is quite sensitive to ambient conditions and is known to undergo chemical modifications. In order to obtain a contamination free surface, the BP crystal has been cleaved under ultra high vacuum conditions.

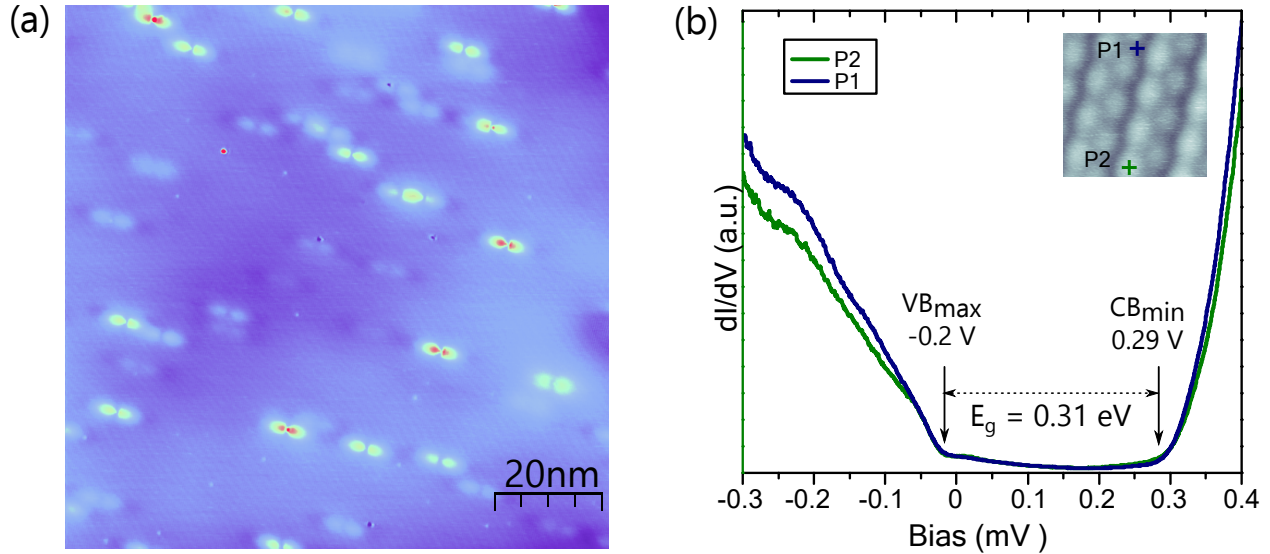


Figure S1: (a) STM topography of pristine BP sample with native defects [$V = -1.0V$, $I = 100$ pA]. (b) Low range STS measurement on the pristine BP surface.

In the figure-S1(a), a representative large area scan of BP surface is shown. Pristine BP regions can be clearly seen in this topography scan, along with the presence of dumbbell shaped defects. Here, we also observe the sub-surface dumbbell defects which can be identified by a weaker contrast compared to the surrounding area, and has been studied by Kiraly et.al. in great detail.¹⁰ Our BP sample is p-doped as observed in the tunneling spectroscopy (STS) measurements presented in Figure-S1(b). The two curves in the plot represent the STS taken at different points in the atomic lattice, as shown in the inset. The band gap is around 0.31 eV which is consistent with the values reported for bulk BP in previous STM studies.¹⁰⁻¹⁴

Switching from defect-B to defect-B'

An electrical pulse from the STM tip changes the properties of **B** type defect. For this experiment, first the tip is parked atop the **B** defect with tunneling parameters- 100 pA and 1.0 V ; then the voltage is ramped up from 1.0 V to 10 V with a voltage step of 4 mV keeping the feedback loop active (i.e. constant current mode). For each point of the spectrum, the accumulation time was 6 ms with a waiting time of 10 s before measurement. In Fig-S2 we show the change in the apparent tip height (labeled as z) in the range- 4.1 V to 4.8 V where the switching takes place.

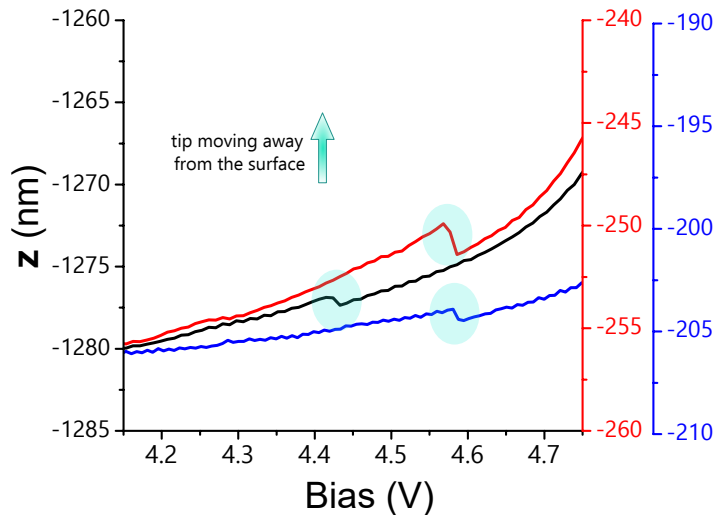


Figure S2: Apparent tip height during the switching of defects of type-**B**

We can observe the switching event (see highlighted circled region in the figure) from the kink in the trace of the tip position as a function bias voltage. In all cases, we find that the movement of the tip is towards the sample (i.e., the tip-sample separation decreases) when the switching occurs. This is in agreement with the observed STM images of defect-**B'** at positive bias, which are imaged with darker contrast (lower LDOS) compared to the brighter contrast (higher LDOS) for a **B** defect. Thus, at the switching bias the tip adjusts the

constant current from a higher LDOS state to lower LDOS state forcing it to move closer to the sample. We also performed the same experiment on the **B'** defect but no changes were observed implying that the transformation is irreversible.

Comparison of defect-A and defect-B'

From STM topography images, such as the ones shown in Fig. 2(a)-(d) in the main text, it appears that **B'** defects bears more resemblance to an **A** type defect. For example, we can observe the contrast reversal feature with bias, as well as the dumbbell shape in negative bias. However, there are some minute differences that can be found after having a closer look at the linescan comparison between these two defect types. In the figure below (Fig S3), we show such a comparison taken in the same area (and at same bias, -0.4 V), corresponding to Fig 2(c) of the main text.

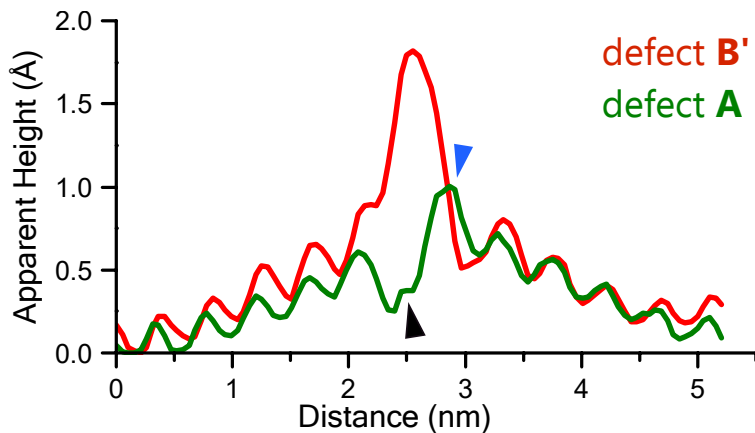


Figure S3: line scan comparison for defects **A** and **B'**, at -0.4 V.

Both defects are identified by a bright spot in the center, though the **B'** defect has a higher contrast (LDOS) compared to the other. Similarly, in the positive bias, a small brighter spot is observed in the center of the defect **B'** which has been shown in Fig 2 (e) of the main text. Defect **A** is identified by only a circular dark region and without any bright spots in the center.

In the linescan profile of defect **A** (green curve), we also show the position of the features:

dark spot (black marker) near the *bright spot* (blue marker) as a visual aid.

Defects Considered in DFT Calculations

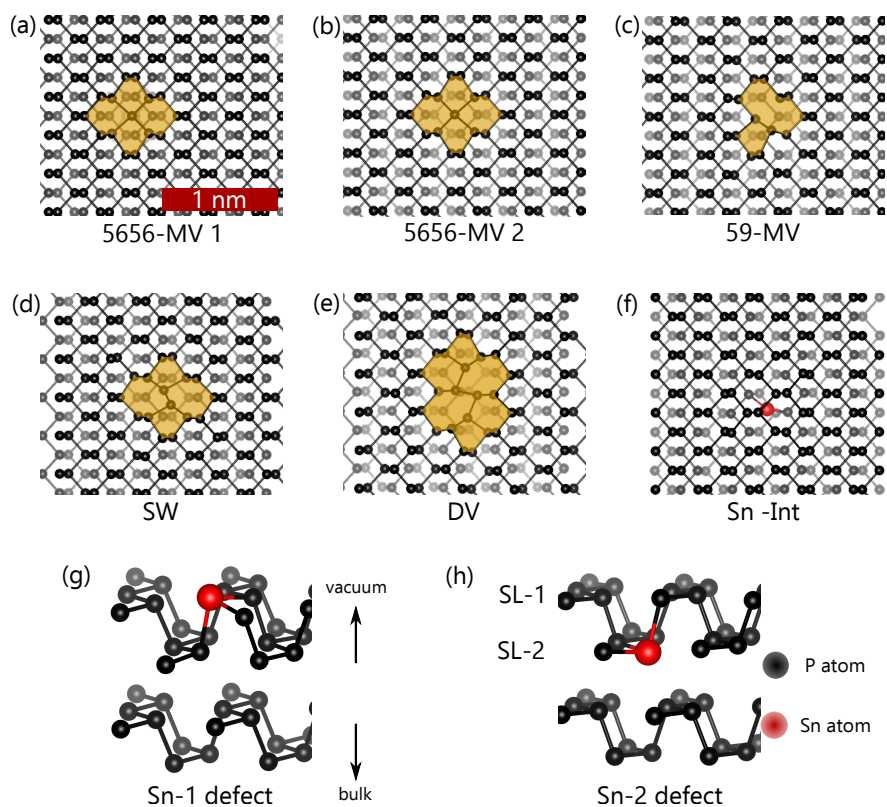


Figure S4: **Relaxed structures of different types of defects considered as possible candidates to be defect-A (as obtained from DFT calculations).** (a) 5656 monovacancy (MV 1) in the upper sub-layer (SL 1), (b) 5656 monovacancy (MV 2) in the lower sub-layer (SL 2), (c) 59 monovacancy, (d) Stone-Wales (SW) defect, (e) Divacancy (DV), (f) Sn interstitial, (g) Sn substituted in SL-1 (Sn-1), and (h) Sn substituted in SL-2 (Sn-2). Panels (a)–(f) show top views (drawn to the same scale), while (g),(h) show side views. Black and red spheres indicate P and Sn atoms, respectively. Yellow colored regions highlight areas displaying local atomic rearrangement in the vicinity of the defect.

XPS data

Below we identify the core level XPS information on the elemental composition for the black phosphorus sample used for the STM/STS measurements.

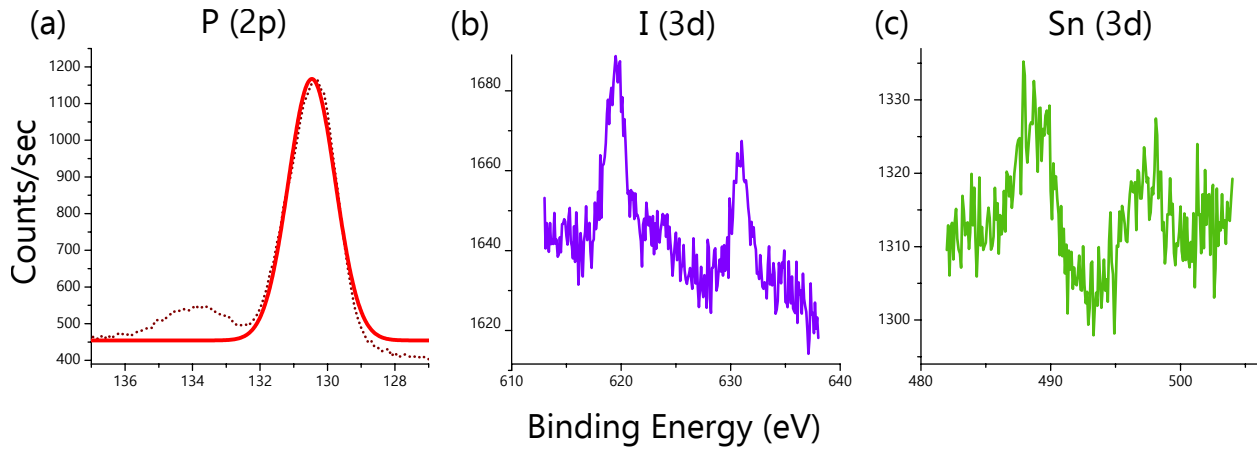


Figure S5: XPS data on BP

XPS measurements were performed in the UHV chamber with base pressure of 2×10^{-10} mbar using Mg K- α non-monochromated X-ray source and Phoibos 100 photoelectron analyzer. Prior to the measurements the samples were cleaved in the loadlock at a pressure of 5×10^{-8} mbar and immediately moved into the main chamber. The cleaving process is the same as performed before STM measurements in the UHV environment.

DFT Results for System with 5656-monovacancy

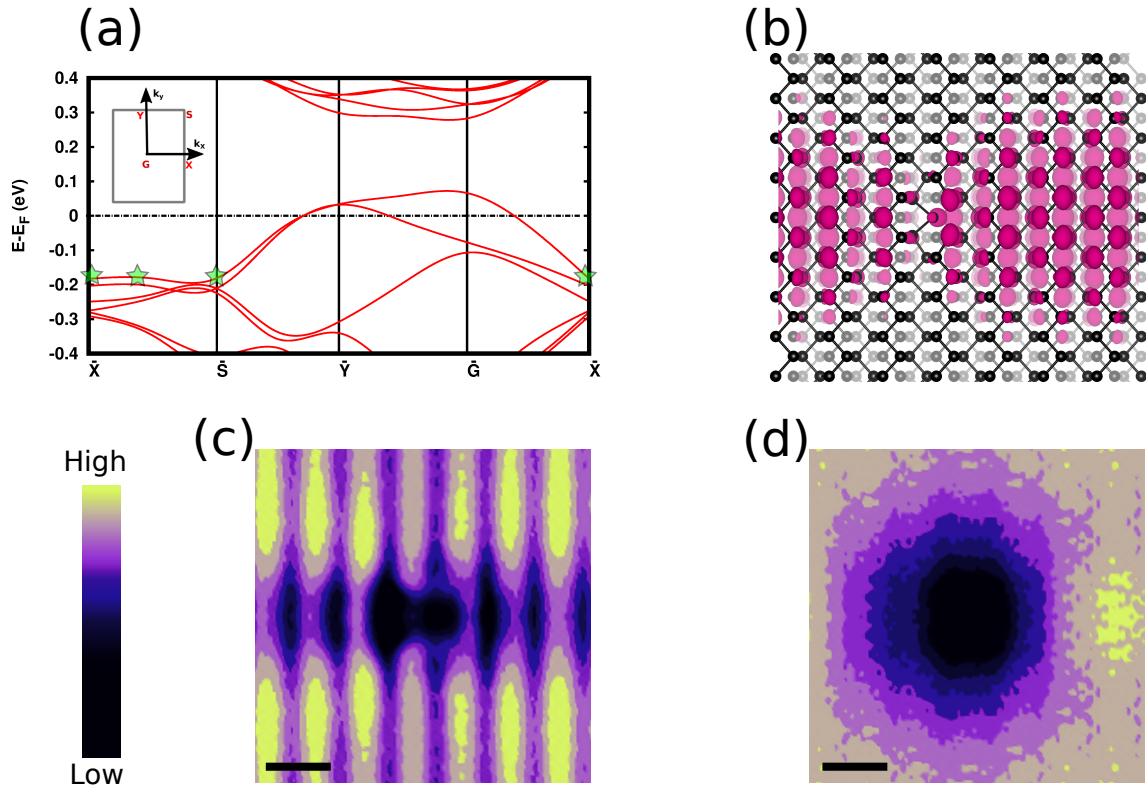


Figure S6: **DFT Results for the System with a Monovacancy labeled 5656-MV-1** (a) Band structure along the path X-S-Y-G-X. (Inset: first Brillouin zone for the black phosphorus supercell used) (b) Band resolved charge density profile at **S** **k**-point for the valence band (indicated with a green star in the band structure plot). Note that the band resolved charge density for all three points marked by green stars has a similar spatial profile. Isosurface value used: 5×10^{-5} e/Bohr³. Panels (c) and (d) are simulated constant current STM images (isosurface = 5×10^{-9} e/Bohr³) for 5656-MV-1 at -0.16 V and $+1.0$ V.

Contributions from p_z orbitals to STM images of BP
with an Sn-int defect.

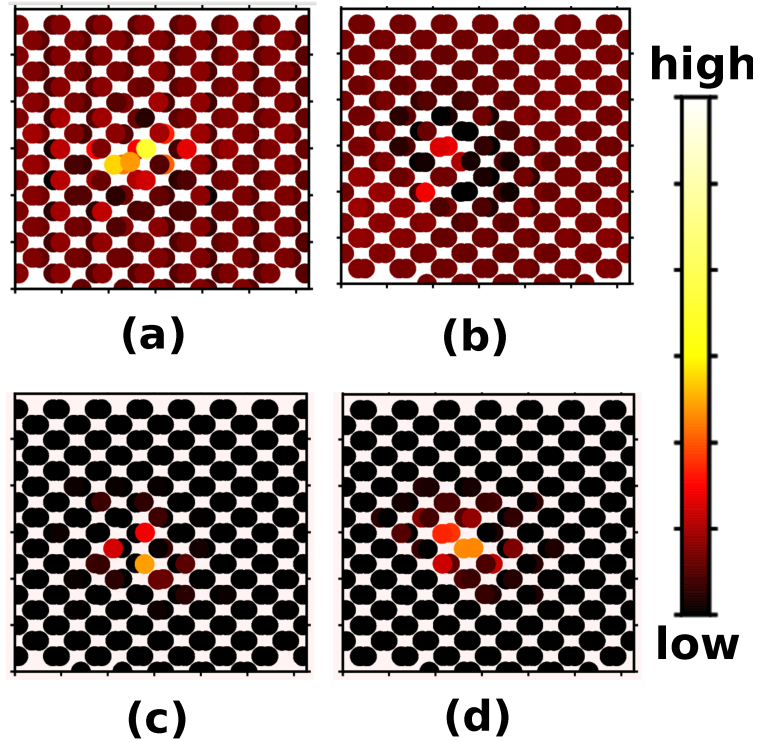


Figure S7: SPOIL plots for Sn-int defect. Panels (a) and (b) show the SPOIL plots for layer 1 and layer 2 at $V = -0.88$ eV. Panels (c) and (d) are the SPOIL plots for layer 1 and layer 2 at $V = +0.53$ eV. Atoms are colored according to the value of $D_{i,j}$, where $j = p_z$. White color represents the highest contribution of p_z and black color of the panel represents the lowest contribution of p_z .

Experimental and calculated STM images of defects **B** and **B'**

In Fig. S8 we show a side by side comparison of experimental and simulated STM images of defects **B** and **B'**. We reproduce the simulated STM images from Fig. 5 that are compared to experimental images.

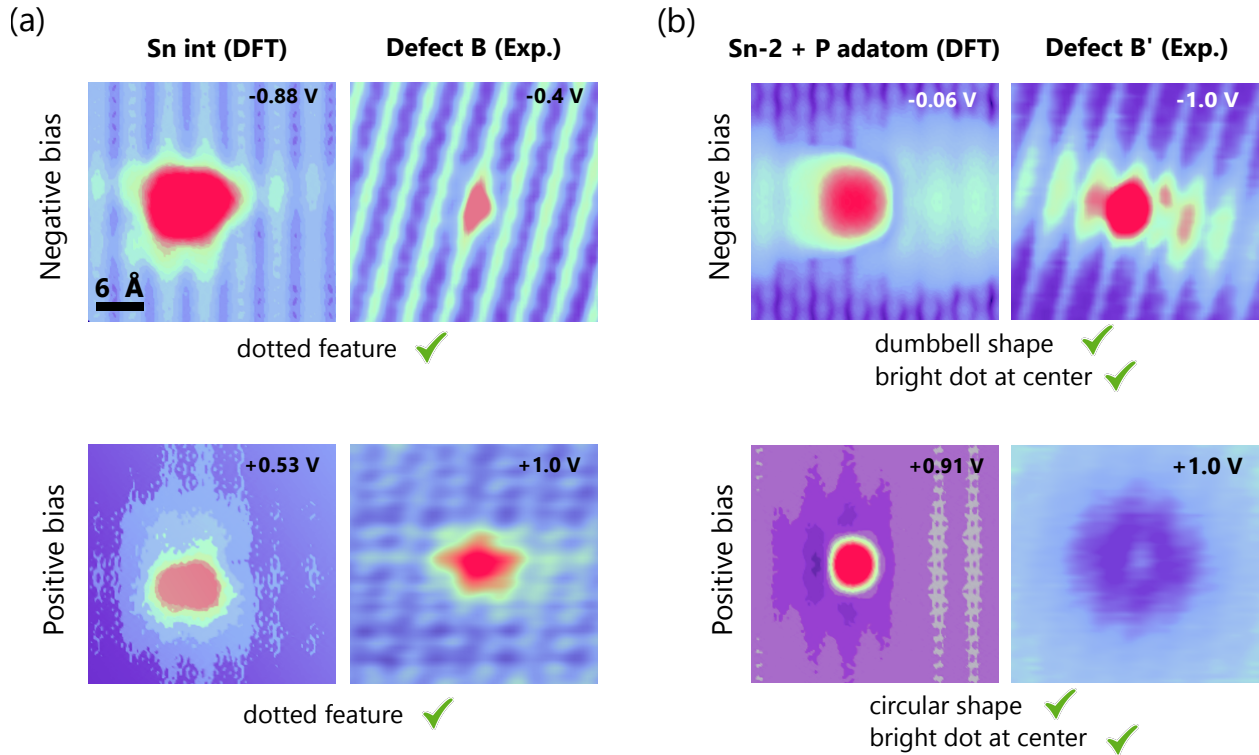


Figure S8: (a) Simulated STM images of a interstitial Sn defect at positive and negative bias (left). Experimental STM image of defect **B** at positive and negative bias (right). (b) Simulated STM images of Sn-2+P-adatom at positive and negative bias (left). Experimental STM image of defect **B'** at positive and negative bias (right).

Defect Formation Energy (DFE):

The defect formation energy is computed as: $DFE = - (E_{pristine} - \sum n_i \mu_i + \sum m_j \mu_j - E_{defect})$, where $E_{pristine}$ is the total energy of the pristine three-layer phosphorene (3L-BP), and E_{defect} is the total energy of the of defected system. n_i is the number of P atoms that are missing from the system due to intrinsic or extrinsic defects, and m_j is the number of substituted/adatoms (e.g., Sn) which cause extrinsic defects. μ_i and μ_j are the chemical potentials of the i^{th} and j^{th} types of atoms, respectively. μ_i for P is calculated by dividing the total energy of pristine 3L-BP by the total number of atoms present in the system. In the case, where Sn is substituted or added to the systems, μ_j is the total energy calculated for an isolated Sn atom in vacuum. The DFE for all three types of defects is tabulated below:

Defect system	DFE (eV)
A (Sn-2)	-3.10
B (Sn-interstitial)	-0.97
B' (Sn-2+P-adatom)	-5.24

References

1. Horcas, I.; Fernández, R.; Gómez-Rodríguez, J. M.; Colchero, J.; Gómez-Herrero, J.; Baro, A. M. WSXM: A software for scanning probe microscopy and a tool for nanotechnology. *Rev. Sci. Instrum.* **2007**, *78*, 013705.
2. Giannozzi, P.; Baroni, S.; Bonini, N.; Calandra, M.; Car, R.; Cavazzoni, C.; Davide Ceresoli,; Chiarotti, G. L.; Cococcioni, M.; Dabo, I.; Corso, A. D.; Gironcoli, S. d.; Fabris, S.; Fratesi, G.; Gebauer, R.; Gerstmann, U.; Gougoussis, C.; Anton Kokalj,; Lazzeri, M.; Martin-Samos, L. *et al.* QUANTUM ESPRESSO: a modular and open-source software project for quantum simulations of materials. *J. Phys. Condens. Matter* **2009**, *21*, 395502.
3. Giannozzi, P.; Andreussi, O.; Brumme, T.; Bunau, O.; Nardelli, M. B.; Calandra, M.; Car, R.; Cavazzoni, C.; Ceresoli, D.; Cococcioni, M., *et al.* Advanced capabilities for materials modelling with Quantum ESPRESSO. *J. Phys. Condens. Matter* **2017**, *29*, 465901.
4. Perdew, J. P.; Burke, K.; Ernzerhof, M. Generalized gradient approximation made simple. *Phys. Rev. Lett.* **1996**, *77*, 3865.
5. Vanderbilt, D. Soft self-consistent pseudopotentials in a generalized eigenvalue formalism. *Phys. Rev. B* **1990**, *41*, 7892.
6. Grimme, S. Semiempirical GGA-type density functional constructed with a long-range dispersion correction. *J. Comput. Chem.* **2006**, *27*, 1787.
7. Monkhorst, H. J.; Pack, J. D. Special points for Brillouin-zone integrations. *Phys. Rev. B* **1976**, *13*, 5188.
8. Marzari, N.; Vanderbilt, D.; De Vita, A.; Payne, M. C. Thermal contraction and disordering of the Al(110) surface. *Phys. Rev. Lett.* **1999**, *82*, 3296.

9. Tersoff, J.; Hamann, D. R. Theory of the scanning tunneling microscope. *Phys. Rev. B* **31**, 805.
10. Kiraly, B.; Hauptmann, N.; Rudenko, A. N.; Katsnelson, M. I.; Khajetoorians, A. A. Probing single vacancies in black phosphorus at the atomic level. *Nano lett.* **2017**, *17*, 3607–3612.
11. Qiu, Z.; Fang, H.; Carvalho, A.; Rodin, A.; Liu, Y.; Tan, S. J.; Telychko, M.; Lv, P.; Su, J.; Wang, Y., *et al.* Resolving the spatial structures of bound hole states in black phosphorus. *Nano lett.* **2017**, *17*, 6935–6940.
12. Tian, Z.; Gan, Y.; Zhang, T.; Wang, B.; Ji, H.; Feng, Y.; Xue, J. Isotropic charge screening of anisotropic black phosphorus revealed by potassium adatoms. *Phys. Rev. B* **2019**, *100*, 085440.
13. Wentink, M.; Gaberle, J.; Aghajanian, M.; Mostofi, A. A.; Curson, N. J.; Lischner, J.; Schofield, S. R.; Shluger, A. L.; Kenyon, A. J. Substitutional tin acceptor states in black phosphorus. *J. Phys. Chem. C* **2021**, *125*, 22883–22889.
14. Fang, H.; Gallardo, A.; Dulal, D.; Qiu, Z.; Su, J.; Telychko, M.; Mahalingam, H.; Lyu, P.; Han, Y.; Zheng, Y.; Cai, Y.; Rodin, A.; Jelínek, P.; Lu, J. Electronic self-passivation of single vacancy in black phosphorus via ionization. *Phys. Rev. Lett.* **2022**, *128*, 176801.